

See discussions, stats, and author profiles for this publication at: <https://www.researchgate.net/publication/51820722>

Generation of Ultra large Surface Enhanced Raman Spectroscopy (SERS)–Active Hot–Spot Volumes by an Array of 2D Nano–Superlenses

ARTICLE *in* ANALYTICAL CHEMISTRY · NOVEMBER 2011

Impact Factor: 5.64 · DOI: 10.1021/ac201712k · Source: PubMed

CITATIONS

3

READS

42

3 AUTHORS, INCLUDING:



Zexiang Shen

Nanyang Technological University

412 PUBLICATIONS 11,440 CITATIONS

SEE PROFILE



Malini Olivo

Agency for Science, Technology and Researc...

278 PUBLICATIONS 4,016 CITATIONS

SEE PROFILE

Generation of Ultralarge Surface Enhanced Raman Spectroscopy (SERS)-Active Hot-Spot Volumes by an Array of 2D Nano-Superlenses

Kho Kiang Wei,^{†,‡} Shen ZeXiang,[§] and Olivo Malini^{*,†,‡,||}

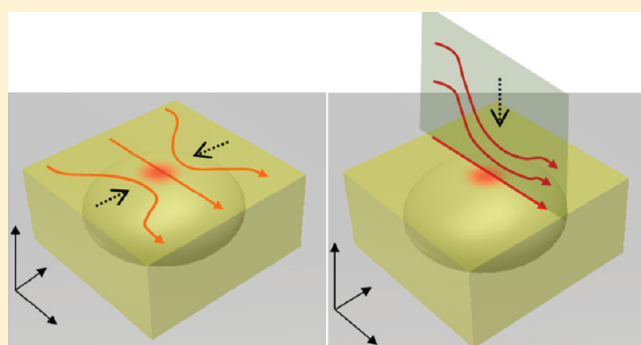
[†]School of Physics, National University of Ireland, Galway, Ireland

[‡]National Cancer Centre of Singapore, Division of Medical Sciences, 11 Hospital Drive, 169610 Singapore

[§]Division of Physics and Applied Physics, School of Physical and Mathematical Sciences, Nanyang Technological University, 21 Nanyang Link, Singapore 637371

S Supporting Information

ABSTRACT: Surface Enhanced Raman Spectroscopy (or SERS) has received tremendous attention in the past three decades. However, the extremely-confined probe volume (1 nm) of the plasmonic hot-spots occurring on a conventional roughened SERS-active metallic surface has limited value in macro-molecular studies. In this article, we show the plausibility of generating large SERS hot-spot volumes on an atomically-flat metal surface based upon a special 3D adiabatic plasmonic nano-focusing effect brought about by an array of nano-scale superlenses. We experimentally demonstrate the feasibility of this particular approach and report, for the first time, the acquisition of whole-protein SERS spectra of a layer of test protein, Cytochrome-c, using a custom-made Otto-Raman spectroscopy system equipped with nano-fluidics. Our study shows the potential of whole-protein SERS spectroscopy as a useful analytical tool that complements surface probe microscopies.



Structural studies of planar macromolecular layers (e.g., protein layers) can provide important insights relating to many cellular functions, such as cell proliferations, cell migrations, wound healing, as well as cell–cell interactions.^{1–3} However, the lack of a suitable technique for such studies has hampered progress.^{4,5} For instance, high-resolution magnetic resonance spectroscopy has restricted use in the study of macromolecular layers under a physiologically relevant condition, owing to the absence of fast tumbling rates.⁶ Additionally, the amorphosity of a typical protein layer prevents the use of X-ray crystallography.⁷ While the atomic force microscopy and the scanning tunneling microscopy have been convenient as a tool for protein studies, they only supply speculative information relating to the internal structures of a protein.⁸ Often, complementary numerical simulations are required to gain structural insights from a surface map.⁵ Unfortunately, there currently exists no reliable experimental means to assist in verifying or in refuting a simulation model. In this article, we demonstrate that it is possible to derive meaningful structural information about a protein layer through the technique of surface enhanced Raman spectroscopy, or SERS. More specifically, we provide a means to expand the otherwise-small (≤ 1 nm) hot-spot volumes of SERS via an array of nano-superlenses, thereby permitting, for the first time, a whole-protein spectroscopic study of a planar macromolecular layer with SERS.

The discovery of SERS has reignited interest in Raman spectroscopy, particularly its use in elucidating a molecular layer. In the conventional dogma of SERS, the enhanced Raman activities

are generally associated with the highly confined surface plasmon fields or SERS hot-spots (SERS-HSs) occurring on a nanostructured metallic surface. As a result, the development of a prudently designed nanostructure has become one of the major focuses in the field of SERS.^{9–12} This has led to the emergence of a plethora of interesting nanostructures, ranging from simple nanospheres,¹³ to nanorods,¹⁴ and to even more complex-shaped particles, such as a star-shaped nanoparticle.¹⁵ Unfortunately, the confined volume of the SERS-HSs in these substrates inevitably restricts SERS to only small molecules (≤ 1 nm).^{16–18} Consequently, larger molecules ($\sim 2–3$ nm or above), such as proteins, can experience SERS only in the parts that are accessible to the SERS-HSs (i.e., the protein surfaces). To overcome this difficulty, Keating et al. demonstrated the feasibility of whole-protein SERS spectroscopy in a protein layer sandwiched in between two plasmonic spherical nanoparticles.¹⁹ In this particular scheme, the large 3D SERS hot-spot volumes are generated in-between electromagnetically coupled nanoparticles, which allows for a whole-protein SERS study with an enhancement factor of up to about 10^{10} .^{19,20} Unfortunately, as this technique requires the protein to be subjected to unphysiologically large compressive forces exerted by the sandwiching nanoparticles, structural instability issues could compound data interpretations;²¹ thus far, no

Received: July 3, 2011

Accepted: November 21, 2011

Published: November 22, 2011

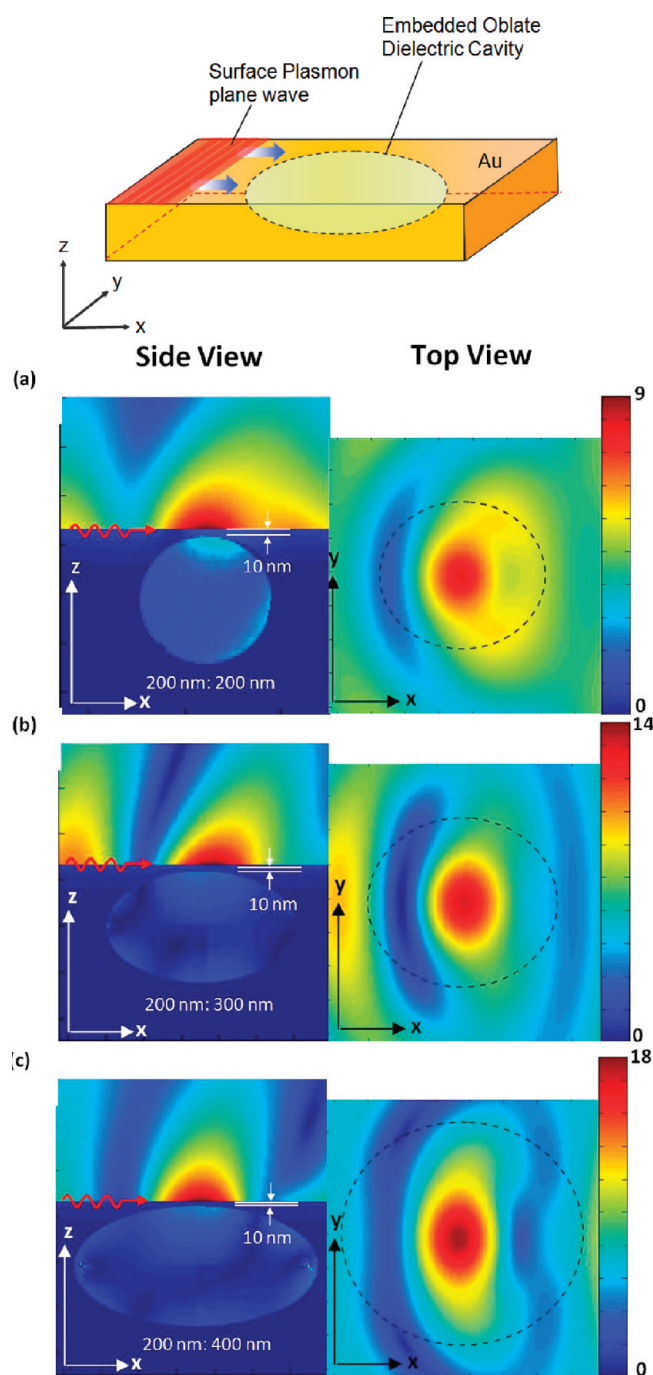


Figure 1. $|E_z|$ map for dielectric nanovoid systems with different void aspect ratios. Dashed circles indicate the position of the buried nanovoids. The void aspect ratios are, respectively, (a) 200/200 nm, (b) 200/300 nm, and (c) 200/400 nm. In each case, the SP (with unit amplitude) is assumed to propagate in the positive x -direction. The nanovoids are assumed to be buried 10 nm beneath the Au surface. Refractive index of the dielectric voids is 1.5, and that of the dielectric bulk above the Au surface is 1.33. Red arrows indicate the direction of the SP.

whole-protein SERS spectrum of physiological relevance has been reliably obtained.²²

Although the manipulation of plasmonic mode volumes has been studied by some previously,^{23–25} their applications in SERS macromolecular study has thus far been overlooked. Here, we report the generation of large SERS-HS volumes without the use

of sandwiching plasmonic nanoparticles. Our method differs from Keating et al.'s approach in that large SERS-HSs are produced not on nanoprotusions or 3D nanostructures as studied in refs 24 and 25, but on an atomically flat metal surface containing a 2D array of nanoscale superlenses. More specifically, we study the relationship between the field enhancements and the mode volumes derivable from a superlens system. On the basis of our previous study of a special adiabatic plasmonic nanofocusing effect brought about by a macroscopic-scale superlens consisting of oblate dielectric voids embedded just beneath a planar metal surface,⁴ we show that a similar focusing effect can also occur at nanoscales (i.e., in oblate dielectric nanovoids as will be discussed in the next section). The Raman enhancement factor achievable with our substrates is over 100 times higher compared with that attainable in a smooth semi-infinite metal bulk. Furthermore, the resultant SERS-HSs are found to be $(38)^3 \text{ nm}^3$ in size, and at least 8 times as large as the conventional SERS-HSs (e.g., those attainable with single metal nanoparticles), rendering it suitable for the structural study of protein layers. To demonstrate the latter point, we have fabricated the above-mentioned nano-superlens system through a cryogenic-stripping approach and experimentally studied the conformational state of a test protein, cytochrome-*c*, bound to the planar surface of our substrate. Measurements were achieved using a homemade Raman-spectroscopy system equipped with polydimethylsiloxane (PDMS) nanofluidics in an Otto-configuration. For the first time, whole-protein SERS spectra are obtained from an atomically flat Au surface, opening up to the possibility of a combinatorial approach to studying a protein layer, using both surface probe microscopy and SERS. The omission of sandwiching plasmonic nanoparticles would permit macromolecules to be studied in a more physiologically relevant condition. The current study could thus contribute significantly to the biomedical fields relating to, say, protein–surface interactions, or to the unfolding mechanism of bound proteins.

THEORETICAL RESULTS AND METHODS

Theoretical Analysis. To illustrate the generation of SERS-HSs by a single oblate dielectric nanovoid embedded just beneath a metal surface, we numerically compute the Maxwell solution of a nanovoid system as shown in Figure 1 (top left, and see also section S1 in the Supporting Information (SI)). The propagating surface-plasmon (SP) is launched with an Otto-setup,³ and assumed to direct along the x -axis. The bury depth, h (i.e., the distance between the top to the void and the planar metal surface), of the nanovoid is set at 10 nm. The validity of the results was verified by asserting that boundary conditions were satisfied at all metal–dielectric interfaces. Note that only the transverse SP-field component (i.e., $|E_z|$) is considered in Figure 1 as the others are generally weak, and contribute negligibly to the overall Raman enhancement.

Interesting observations can be made when the aspect ratio of the embedded void is varied (see middle and right columns in Figure 1). In particular, the field-enhancement factor, FEF [defined as the ratio of the local $|E_z|$ on the metal surface to the incident amplitude $|E_i|$, i.e., $\text{FEF} = (|E_z|)/(|E_i|)$], was found to increase with increasing major diameter of the void, accompanied concomitantly by a reduction in the volume of the SERS-HSs. A comparison of the modal volumes and field enhancements achievable in the current system and various other plasmonic

nanostructures is included in the SI (see Tables 2 and 3 in section 2 of the SI).

Such a characteristic is summarized in Table 1 and is found to be closely connected to the mechanisms behind the formation of the SERS-HSs at the thin metal film region (TF in Figure 2a) situated between the top of the embedded void and the planar metal surface. To elucidate this point, we draw a parallelism between the TF and an asymmetric Au film. We recall the thin-film dispersion curves as shown in Figure 2b. Note that, in calculating this graph, it has been assumed that the film is sandwiched between a water medium ($\varepsilon = 1.77$) and a polymer medium ($\varepsilon = 2.25$) so as to reflect the environment seen by the TF in Figure 2a. It is clear, from the dispersion plot, that, for any given k_{sp} , two SP modes are possible on a Au film: a symmetric

Table 1. Maximum Achievable Field Enhancement Factor (FEF) and Plasmon Hot-Spot Width for Different Void Aspect Ratios

| void aspect ratio (minor major) | FEF | fwhm (nm) |
|---------------------------------|-------|-----------------|
| 200 nm/200 nm | 10.03 | 85 ^a |
| 200 nm/300 nm | 13.37 | 83 |
| 200 nm/400 nm | 18.07 | 78 |

^a Lateral dimension of the SERS-HS fields calculated at full-width half-maximum (fwhm).

SP mode (S_b) characterized by the charge of equal sign accumulating on both sides of the film as depicted in Figure 2b, and generally exhibiting a low phase velocity, i.e., long SP wavelength, or a higher-momentum (i.e., shorter SP wavelength) antisymmetric SP mode (a_b) in which charge signs (see illustration in Figure 2b) are opposite on both sides of the film. By examining the directionality of the $E \rightarrow_z$ fields near TF, we found the SERS-HSs so-produced to be of the a_b -type, implying a coupling to higher-momentum a_b -SP modes as the incident SP wave enters the TF region, which leads to increases in the SP energy densities there, i.e., formation of hot-spot (see right panel in Figure 2a). While the momentum mismatches between the incident-SPs and the a_b -SPs could potentially elicit backscatterings of the SP-wave, a gradual thinning of the TF “thickness” toward the minor axis of the void (see left panel in Figure 2a) ensures a reflection-free (i.e., adiabatic) coupling and results in the generation of an extremely intense SERS-HS. The area under which the nanovoid is buried thus behaves as a nanoscopic superlens.⁴ Pyonting vector maps shown in Figure 2c,d further elaborate such an energy-focusing mechanism. Here, a 200/400-nm oblate dielectric void is considered because of its large FEF. The energy flows are depicted with normal Pyonting vectors defined as $\vec{p} = (1/2)[\text{Re}(\vec{E} \times \vec{H}) / \text{Re}(\vec{E} \times \vec{H})]$. From the map, it is evident that two types of focusing events prevail. First, a lateral focusing of the SP energy (see right panel of Figure 2c) is manifested by vectorial changes

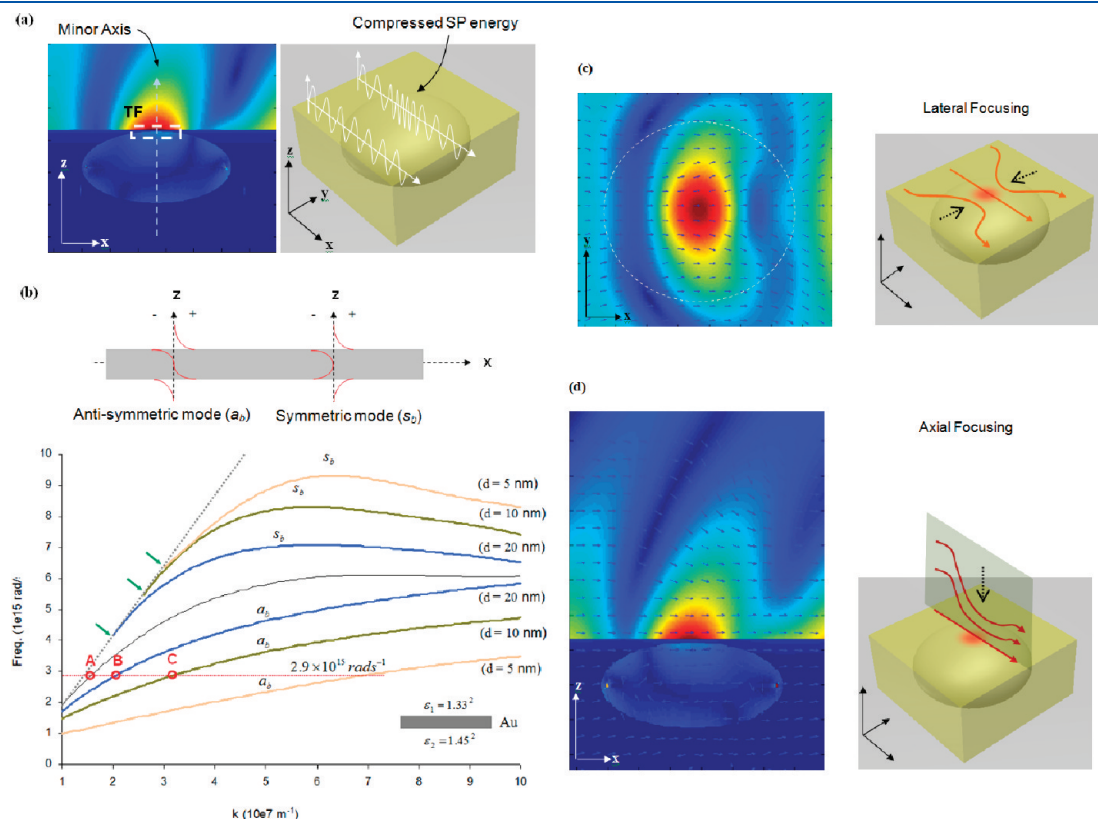


Figure 2. Change in the phase velocity of SP traversing across the thin layer above the embedded dielectric spheroidal nanovoid. (a) Illustration of SP wavelength compression by the thin layer. (b) Dispersion of plasmonic modes on a Au film for various values of film thickness. The dashed curve represents the allowable plasmonic modes on the surface of a semi-infinite Au film. Colored curves are the dispersions for various thin metal films. Curves above and below the dashed curve correspond, respectively, to the antisymmetric and symmetric plasmonic modes on the film. Film thicknesses are indicated in the graph. Data are calculated on the basis of the EM theory of a 3-layer stratified system. Dielectric constants of Au are evaluated using the experimental data obtained by Johnson and Christy. The dielectric constants for the mediums on both sides of the film are, respectively, 1.77 and 2.25. (c, d) Pyonting vector maps showing the direction of optical energy flow in the 200/400-nm void system. Incident SP is assumed to propagate in the positive x -direction.

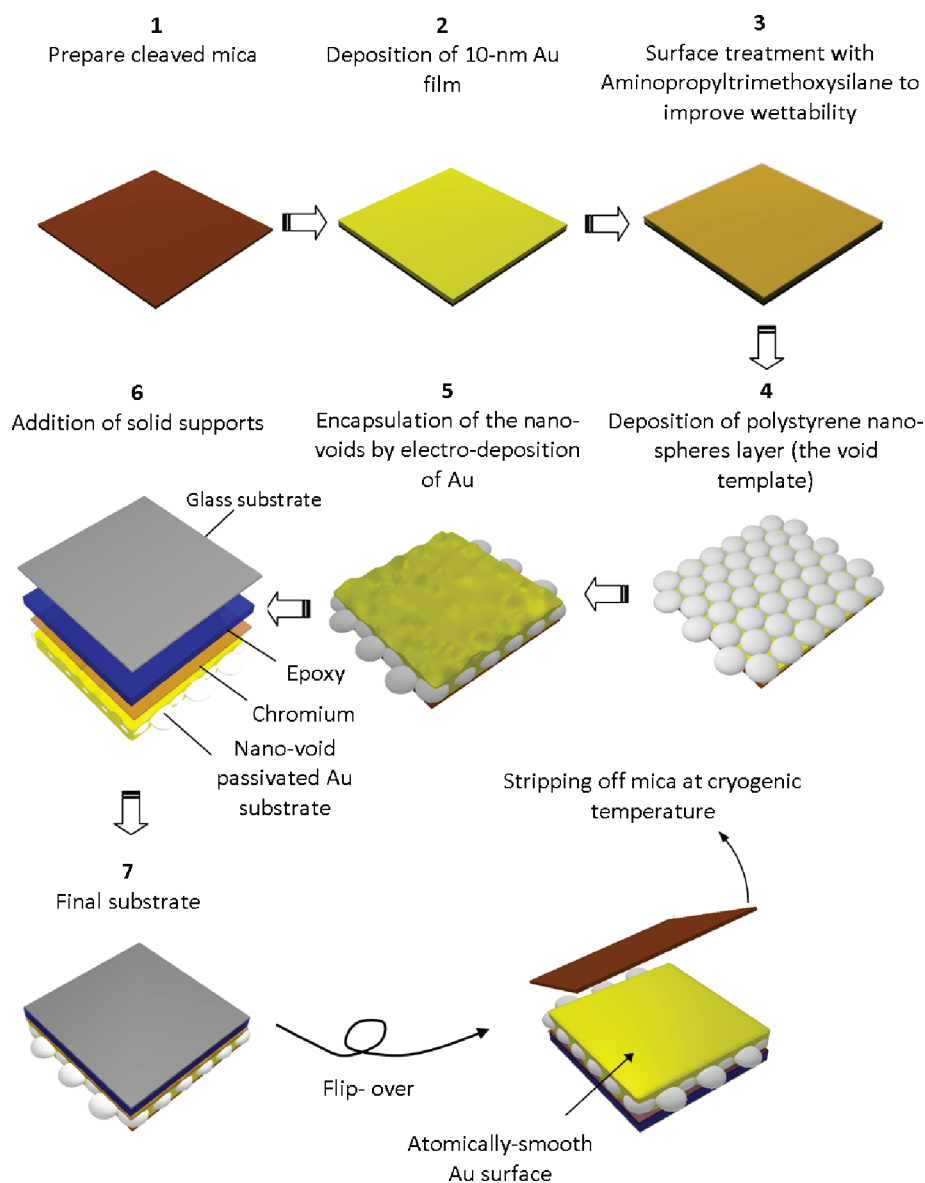


Figure 3. Fabrication scheme.

in the k_{xy} of the SP wave traversing across the TF above the void, in a manner akin to the focusing of a parallel light beam by a high refractive-index cylindrical lens. Second, an axial compression of the SP energy occurs due to the large momentum, k_{xy} , and, hence, large imaginary k_z of the a_b -SPs at the TF (see Figure 2d). One can therefore view the creation of the SERS-HS as a form of “3D nanofocusing” of the SP energy.

A beneficial consequence of such a focusing effect is the production of large SERS-HS volumes, which are about 8 times as large as those achievable in conventional SERS substrates (see section S2 in the SI). In the subsequent sections, we will demonstrate the use of such a large SERS-HS volume for the Raman spectroscopic study of a protein.

Fabrication of Metal Substrates with Embedded Spheroidal Nanovoids. A detailed description of the fabrication method is included in section S3 of the SI. The fabrication steps are also depicted in Figure 3. As can be seen, a top-down cryogenic-stripping approach is used to produce a Au-void system with an ultrasmooth surface, which is essential in promoting the

3D-nanofocusing effect by minimizing unwanted in-plane SP scatterings arisen from involuntary surface roughness.²⁶ Contrary to the conventional electrochemical encapsulation scheme for producing void-filled metal films, the current method involves forming the capping metal surface first on a flat template (e.g., mica) prior to the encapsulation of the nanovoid template (see steps 4–5). In this way, the capping surface can be made extremely flat, and not affected by the encapsulation process. As shown in the figure, the fabrication process begins with a Au film deposited on the ultrasmooth (110) plane of a cleaved mica substrate (see steps 1–2 of Figure 3). The side on which the film is contacting the mica template will eventually become the “capping” metal surface after mica strip-off (see step 7). Thus, the roughness of the final capping surface is determined entirely by that of the mica template, which is usually at the atomic level. Additionally, the deposited Au film also acts as a spacer that determines the distance, and hence the depth, of the embedded nanovoids from the planar capping metal surface in the final substrate. In the current study, this initial Au film’s thickness was

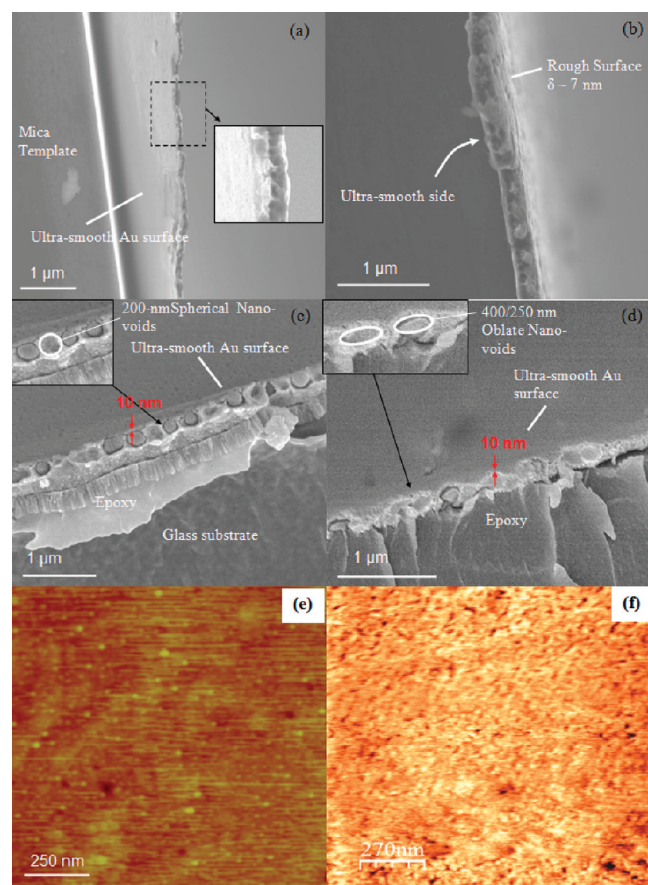


Figure 4. Cross-sectional FE-SEM images of NV-Au substrates: (a, b) free-standing NV-Au films, (c) film containing 200-nm spherical nanovoids, (d) film containing 200/400 nm oblate nanovoids. (e, f) AFM and STM scans of the stripped Au surface, respectively. In parts c and d, the void-passivated metal films were glued onto glass substrates before sectioning in order to maintain structural integrity. AFM measurements were performed under ambient conditions using a Digital Instrument DI3000 Nanoscope III in tapping mode (247.9 kHz) with a typical resolution of about 5–15 nm, and a horizontal scanning rate of 1 Hz. STM image was obtained in an ultrahigh vacuum (UHV) system (base pressure 5×10^{-11} Torr) equipped with a room-temperature (RT) STM. The scanning voltage was -3.5 V, and tunneling current was -100 pA.

chosen to be 10 nm, which was thick enough to maintain a hole-free continuous film, but thin enough to keep the void-to-surface distance well within the penetration depth (~ 25 nm) of the SPs. The void template was consisting of a monolayer of closely packed (but not necessarily hexagonal) polystyrene spheroidal (spherical or oblate) nanoparticles deposited via the method of convective self-assembly (see section S3 in SI for more details). Two different types of polystyrene nanoparticles were used in the current study: 200-nm spherical nanospheres; 200/400 nm oblate nanoparticles. Following the encapsulation of the nanovoid template by electrodeposition of Au, the mica template was stripped off to reveal the smooth capping surface. It is crucial that the stripping be clean, i.e., without leaving behind any residual mica shard on the exposed Au surface. To achieve this, we induced a differential contraction between the Au surface and the mica template by soaking the final substrates in liquid N_2 for 2 min. This allowed the mica to detach from the Au, and to be

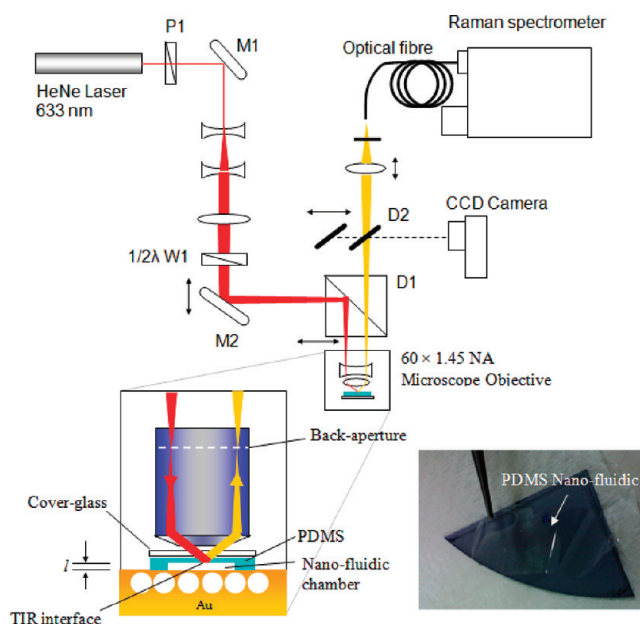


Figure 5. Schematic diagram of an Otto Raman system used in the current study. Laser wavelength = 633 nm. Output power = 17 mW. TIR objective lens: 60×1.45 NA. Incident angle at the TIR interface can be varied by adjusting M2 as indicated by the double-headed arrow.

peeled off conveniently either with a tweezer or cellophane tape. Figure 4a,b shows typical cross-sectional FE-SEM images of the nanovoid passivated Au substrates (NV-Au). Figure 4c,d shows cryogenic-stripped samples containing 200-nm spherical nanovoids and 200/400-nm oblate nanovoids, respectively.

We note that the void-to-surface distance in both samples is measured to be about 10 nm, which corroborates well with the thickness of the initial Au film deposited on the mica. A typical AFM surface scan across the exposed Au, underneath which nanovoids were buried, is shown in Figure 4e, revealing an atomically flat morphology with an average roughness not exceeding 0.55 nm (rms). A high-resolution mapping obtained using a scanning tunneling microscope (STM) at a constant-current mode shows the cryogenic-stripped Au surface to be generally hole-defect free as depicted in Figure 4f. The surface roughness estimated through STM is found to be 0.45 nm (rms), which is in agreement with that derived from AFM measurements. The absence of hole defects in the cryogenic-stripped samples represents another advantage of the current fabrication approach because hole defects could inevitably couple incident waves to surface plasmons, bringing about undesired plasmonic ring modes, or giving rise to radiative loss.

Otto Total-Internal-Reflection (TIR) Configuration with PDMS Nanochamber. Detailed description of our Raman microscopy system can be found in section S4 in the SI. Due to the thickness of the NV-Aus, we couple the incident fields to the propagating SP via an Otto configuration provided by the PDMS ($\eta = 1.45$) nanofluidic chamber as shown in Figure 5. The chamber was casted from a Si mold and was sandwiched between a cover-glass and the NV-Au substrate (see photo and the cartoon illustration in Figure 5, and sections S4 and S5 in the SI for fabrication details). The liquid-gap ($\eta = 1.33$) separation, l , between the TIR interface and the smooth surface of the NV-Au is about 300 nm, which is the optimal distance estimated for an efficient light-to-SP coupling (see section S4 in the SI). A small

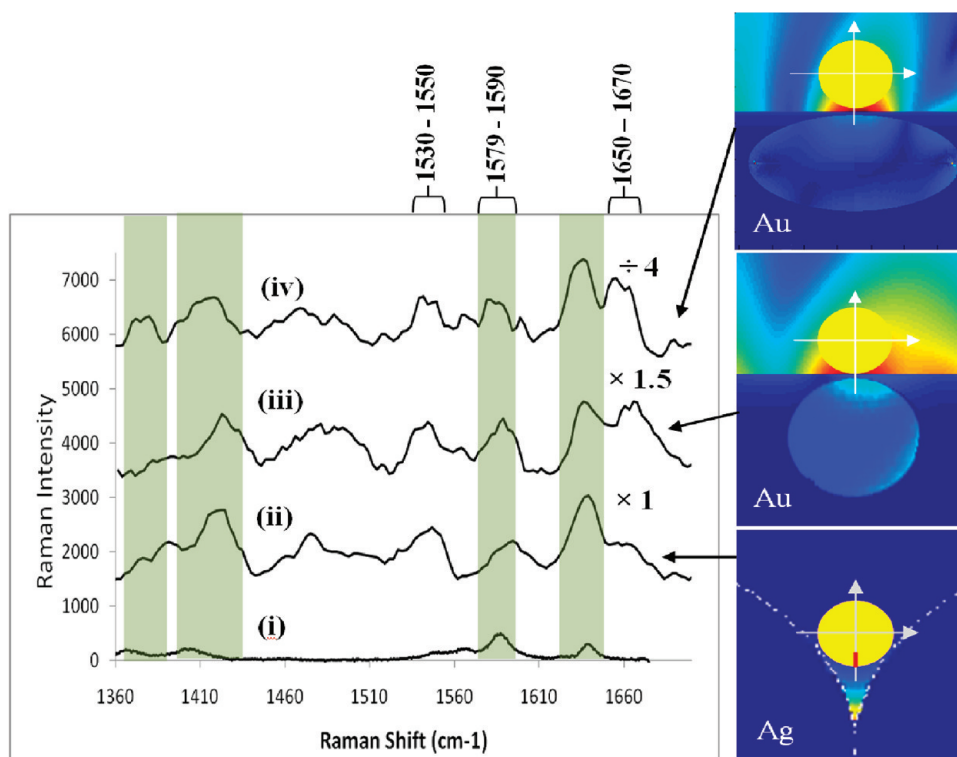


Figure 6. Whole-protein SERS spectra of the cytochrome-c protein. (i) Resonance Raman spectrum obtained at 514 nm (acquisition time = 20 s). (ii, iii, iv) SERS spectra derived from Ag-FON, 200-nm spherical NV-Au, and 200/400 nm oblate NV-Au, respectively. The acquisition time for spectra ii–iv is 100 s. The insets on the right illustrate the sizes of the cytochrome-c protein relative (not to scale) to the SERS-active hot-spot volumes on the substrates. Yellow spheres represent cytochrome-c. Note the scaling factors for each of the spectra.

amount of immersion oil was applied to the objective-lens–cover-glass and cover-glass–PDMS interfaces in order to reduce refraction. The same objective lens was also used to collect backscattered light (Rayleigh plus Raman) from the sample. The excitation beam (633 nm, 3 mW) was made to converge, and finally focused, via a dichroic mirror, D1, onto the edge of the back aperture of the objective (see Figure 5) so that the incident beam can undergo a total internal reflection (as shown in the inset) at the TIR interface. Coupling between the excitation light and the SP on the Au surface was established by adjusting the mirror M2 until the totally reflected beam from the TIR interface was dimmed (see also section 6 in the SI for reflectivity scans). A half-wave plate (W1) was used to ensure the excitation beam is p-polarized.

RESULTS AND DISCUSSION

Selection of the Test Protein. In order to demonstrate the advantages of the large hot-spot volumes produced by our NV-Aus in macromolecular study, we judiciously determined the choice of our test protein. Several criteria must be considered in this attempt. First, the selected protein must be well-characterized previously. Second, the protein must be large (say, ≥ 3 nm) and carries a moiety with Raman characteristics distinct from those of the protein bulk (e.g., amide bands). Third, this particular moiety must situate at a known location on the protein surface. Lastly, the protein molecule must exhibit an asymmetric charge distribution that allows it to be oriented in a specific direction with the moiety facing toward the SERS-active metal surface. The latter points are extremely crucial, for they permit

the use of the intensity ratio between the Raman peaks of the protein bulk (particularly, the α -helix amide bands) and those of the moiety as a convenient “ruler” in evaluating the spatial extension of the hot-spot volume: a short-range field will preferentially excite the moiety.

Cytochrome c (Cyto-c), an oblate protein molecule comprising of 104 amino acids with a mean diameter of about 34 (size when binds to hydrophilic surface) Å,^{27,28} appears to be the best candidate. Being a key component in the respiratory pathway of cells, Cyto-c carries a heme-porphyrin moiety that is responsible for the electron transfer in the redox process.^{29,30} This moiety is typically located toward a lysine-rich surface (Lys-25, 27, 72, 79), which, under a neutral-pH condition, becomes positively charged,³¹ thereby permitting the Cyto-c to be oriented in a known direction when adsorbed onto a negatively charged surface (i.e., with the heme positioned in close proximity to the negatively charged surface), e.g., carboxyl-terminated alkanethiol layer on a Au surface.^{31–34}

Functionalization of NV-Aus. All Au SERS-active substrates were rendered negatively charged, through functionalization with an 11-MUA/1-Oct (11-mercaptoundecanethiol/1-octanethiol) monolayer prepared at a mixing ratio of 1:10 ($[MUA]/[Oct]$), which is necessary in order to promote ionization of the carboxyl group.^{35,36} An Ag-FON (Ag-film over nanosphere) was also used to represent a conventional SERS substrate, and was similarly functionalized. The reason for using an Ag-FON instead of Au-FON is its relatively higher SERS enhancement factor. Note that although Ag is generally highly reactive toward organic molecules as compared to Au, there will be no risk of protein denaturation because of the protective alkanethiol layer (~ 0.6 nm).

Acquisition of SERS Spectra with the NV-Aus. Figure 6 shows typical SERS spectra of 1-mM Cyto-c obtained from the Ag-FON (spectrum ii) as well as from the NV-Aus (spectra iii–iv), along with the Cyto-c resonance Raman spectrum derived at 514-nm excitation wavelength (spectrum i). Note that spectrum ii was obtained with a Raman system in an Epi-configuration, while spectra iii and iv are in Otto-configuration (see section 4 in the SI). Except for spectrum i, each of the spectra shown in Figure 6 represent an average of 10 measurements. All spectra were background-corrected using a sixth-order polynomial that set the Raman intensities at 1360, 1435, 1520, 1610, and 1750 cm^{-1} to null. For ease of comparison, spectra ii–iv have been scaled to equalize their spin-marker band's intensities (at about 1636 cm^{-1}). Scaling factors are displayed alongside their respective spectra (see Figure 6). Note that the absolute spectral intensities may vary substantially between different setups, due to variations in the collection efficiency (between the Epi-configuration and the Otto-configuration). We further note that no detectable Raman signals could be observed when the NV-Au was replaced by a reflective smooth Si wafer or a solid Au film, confirming the Cyto-c spectra iii and iv arise from nanovoid induced plasmonic hot-spots, and are not a result of enhanced Raman scatterings from the freely diffusing Cyto-c molecules due to multiple reflections between the TIR interface and the Au surface. Note also that under no conditions could a Raman signal be detected in the absence of the carboxyl-terminated alkanethiol layer, suggesting that the SERS spectra obtained indeed originated from a concentrated monolayer of Cyto-c adhered electrostatically onto the alkanethiol coating.

Analysis of SERS Spectra. Next, we analyze the spectral position of several major bands. All of the heme-related vibrational frequencies, namely the 1370, 1406, 1588, and 1637 cm^{-1} bands (shaded bands in Figure 6), are generally observable. This is expectedly so since the specific orientation of the adsorbed Cyto-c would place the heme-moiety close to the carboxyl-terminated Au surface, as shown by Zhou et al.'s simulation results,³¹ and thus is preferentially excited. Nonetheless, emphasis must be given to the 1635–1637 cm^{-1} band, which is attributable to the heme's spin-marker band characteristic of the protein's integrity.²⁹ While this specific band is located at 1637 cm^{-1} in the Ag-FON-derived Cyto-c SERS spectrum (spectrum ii), which suggests the absence of protein denaturation, a slight downshifting of the spin-marker band to 1634 from 1637 cm^{-1} is observed in the spectra derived from NV-Aus (i.e., spectra iii and iv). We, however, do not conclude this to be a sign of protein damage since the band position remains well above the characteristic 1625 cm^{-1} mark of ligand displacement from the active site of heme.²⁹ Such a shift can be explained by a slight conformational change occurring in the Cyto-c when bound to a planar carboxyl-terminated surface as pointed out by Zhou. It was predicted that the Cyto-c could expand by up to 1.6%,³¹ which might concomitantly perturb, to a small extent, the microenvironment in which the heme resides, and hence the changes in the spin-marker band.

The above conclusion about the conformational state of the adsorbed Cyto-c can be further substantiated by comparing bands at 1530–1550, 1579–1590, and 1650–1670 cm^{-1} in spectra ii–iv, from which one could also infer the SERS-HS field-structure of the NV-Au. We will first focus on the 1650–1670 cm^{-1} band, which is attributable to the amide-I band of the Cyto-c. The preferential appearance of this particular band in spectra iii–iv, i.e., in spectra derived from NV-Au, is especially

Table 2. Fitting Results for Cytochrome-c SERS Spectra^a

| band assignments | AgFON | 200 nm-NPAuSub | 400–200 nm-NPAuSub |
|---------------------------|-------------------------|----------------|--------------------|
| Heine | 1531(0.29) ^b | 1532.59(0.36) | 1534.66(0.40) |
| Trp | 1548.24(0.41) | 1547.05(0.63] | 1547.18(0.57] |
| Trp | 1577.11(0.21) | 1576.95(0.52] | 1571.93(0.53) |
| Heine | 1587.53(0.33) | 1586.55(0.42) | 1583.06(0.43) |
| Heine | 1634(1) | 1633.18(1) | 1634.41(1) |
| α -helix (amide I) | 1648.99(0.23) | 1647.2(0.61] | 1651.98(0.63) |
| β -sheet (amide I) | 1658.6(0.40) | 1659.93(0.61) | 1660.21(0.52] |
| γ -turn (amide I) | 1671.82(0.30) | 1671.11(0.56] | |

^a All intensities shown are normalized to the heme vibrational-peak intensity at "1634 cm^{-1} ": intensity variation = $\pm 10\%$. ^b Wave number (normalized intensity).

interesting. Although this may prompt one to conclude that the observation is a result of the Cyto-c's structure collapsing onto the absorbing surface, thereby leading to the amino-acid chains becoming closer to the Raman-enhancing hot-spots, this scenario however does not concur with the spectral position of the spin-marker band measured here, and is therefore ruled out.

The differences between the amide-I bands in spectra ii and iii–iv, nonetheless, can be explained in terms of the volumes of the SERS-HS fields generated in the NV-Aus and in the Ag-FON. While metal-overcoated nanosphere arrays have been well studied and shown to be highly reproducible,³⁷ the Raman enhancing fields are generally short-range due to the rough surface features.³⁸ SERS enhancement could drop by up to 80% for every nanometer increase in distance from the metal surface. NV-Au, on the other hand, does not suffer from such a shortcoming as its plasmon fields are generally long-range with less than 10% drop in EF for every nanometer increment in the distance of the analyte from the surface (see section S7 in the SI, and Figure 1c). Thus, it is not surprising that the amide I band is more pronounced in the NV-Au-derived SERS spectra compared to that derived in Ag-FON, i.e., a conventional SERS substrate. Although charge-transfers between the Ag and the heme moiety may have resulted in chemical enhancement, and, thus, the preferential appearance of the spin-marker band in the Ag-FON derived spectrum (i.e., spectrum ii), this is fairly unlikely due to the large separation between the Ag and the Cyto-c by the "thick" alkanethiol ($n = 11$) layer.³⁹

To further validate the above electromagnetic explanation, we semiquantitatively analyze spectra ii–iv via curve-fitting. The fitting results are shown in Table 2. The 1530–1550, 1579–1590, and 1650–1670 cm^{-1} bands were, respectively, fitted with two, two, and three peaks. Note that the intensities of all fitting peaks have been normalized to that of the heme vibrational peak at 1634 cm^{-1} in the corresponding spectra. All fitting peaks are Gaussian and narrow, with a bandwidth-at-half-height (bwhh) of 10–20 cm^{-1} , suggesting "tight" and well-formed structures;¹ i.e., the Cyto-c molecules have not been denatured. An increase in the normalized intensities of the 1652 cm^{-1} α -helix amide-I peak observed in spectra iii and iv compared to that in spectrum ii, as indicated in Table 2, implies that the whole bulk of Cyto-c adsorbed on the NV-Au is more uniformly excited due to the "huge" SER-HSs. This argument is followed by the parallel observation of increased contributions from the C2=C3 stretch of the σ_3 normal mode at 1542 and 1577 cm^{-1} of the tryptophan residue (Trp 59) that is situated opposite the heme moiety, and therefore further away from the Au surface.

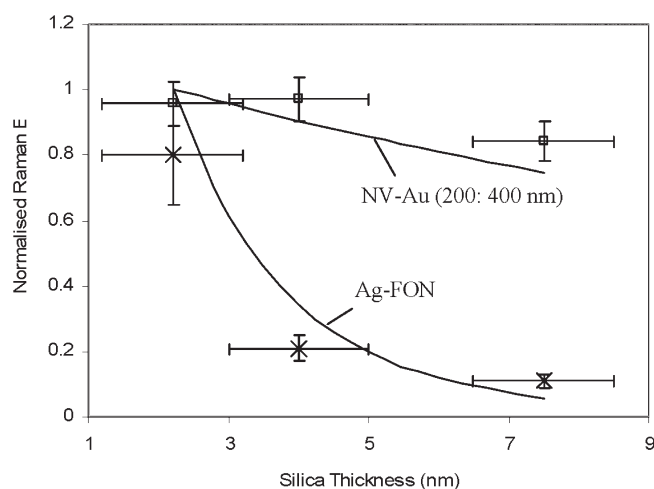


Figure 7. Distance dependence of normalized SERS intensity measured on the NV-Au and Ag-FON. Markers represent experimental data while the solid curves show theoretical values.

We further studied the field decays in the NV-Aus and Ag-FON by observing changes in the SERS intensities of a Raman dye when the metal surfaces were coated with silica films of various thicknesses. Figure 7 shows the decays of normalized SERS peak-intensities of crystal-violet solution ($10 \mu\text{M}$) at 1190 cm^{-1} for silica thicknesses ranging between 2 and 7.5 nm. Differences in the field extension between the two substrates are obvious, with the rapid-decaying Ag-FON curve being mathematically describable by an enhancement-factor equation of the form $EF(z) = C_0(1/(1 + (z - h)/a))$, while $EF(z) = C_1e^{-\beta z}$ for the NV-Aus (see also section S7 in SI). These equations indicate that SERS on the Ag-FON (i.e., the conventional substrate) arises entirely from the short-range localized plasmon fields, whereas that on the NV-Aus is due to focusing of propagating (long-range) SPs by the superlens.

CONCLUSIONS

In conclusion, we have mathematically analyzed the field structures as well as the focusing properties of various plasmonic systems with embedded spheroidal nanovoids. Particularly, we have shown the possibility of 3D adiabatic nanofocusing by nanoscale superlenses. Subsequently, SERS measurements of Cyto-c protein were carried out using our NV-Aus. Our SERS-data and analyses on the spin-marker and amide bands substantiated the electromagnetic simulation results discussed in the second section, especially the generation of large hot-spot volumes by NV-Aus. Finally, the field decays in both the Ag-FON (i.e., the conventional substrate) and the NV-Aus were experimentally studied and were found to have arisen from different types of plasmonic fields. Lastly, it should be pointed out that while the SERS performance of a conventional SERS substrate relies primarily on a small number of highly confined ($<3 \text{ nm}$) but extremely intense plasmonic hot-spots that are scattered on the roughened metal surface, our NV-Aus rely on weaker but larger plasmonic hot-spots (as a result, more molecules are excited, and thus result in an augmented overall Raman intensity). Although field diminutions may occur elsewhere from the nanovoids in our NV-Aus, the fact that SERS enhancements were observed suggests that the field amplifications above the nanovoids are large enough to compensate for such losses.

The current study thus provides a demonstrative example of the use of large hot-spot fields in elucidating the conformational state of adsorbed macromolecules under a physiologically relevant condition.

ASSOCIATED CONTENT

S Supporting Information. Additional information as noted in text. This material is available free of charge via the Internet at <http://pubs.acs.org>.

AUTHOR INFORMATION

Corresponding Author

*E-mail: malini.olivo@nuigalway.ie. Fax: +353-91-494584.

Present Addresses

^{||}Nanophotonics and Biophotonics Group, School of Physics, National University of Ireland, Galway, University Road, Ireland.

ACKNOWLEDGMENT

We would like to thank the Bio-Medical Research Council (BMRC 05/1/31/19/397) for the financial support of this project. The principal author would like to thank Singapore Millennium Foundation (SMF) for the award of postgraduate scholarship. Thanks should also be given to Prof. Subodh Mhaishalkar, Dr. Fan Hai-Ming, Ms. Karen Koh Zhen Yu, Ms. Iman Ahmad, and Mr. Chu Xin Jun for their technical assistances.

REFERENCES

- (1) Engelman, D. M. *Nature* **2005**, 438, 578.
- (2) Willig, K. I.; Rizzoli, S. O.; Westphal, V.; Jahn, R.; Hell, S. W. *Nature* **2006**, 440, 935.
- (3) Barlett, A. I.; Radford, S. E. *Nat. Struct. Mol. Biol.* **2009**, 16, 582.
- (4) Kho, K. W.; Shen, Z. X.; Olivo, M. C. *Opt. Express* **2011**, 19, 2502.
- (5) Makrodimitris, K.; Masica, D. L.; Kim, E. T. *J. Am. Chem. Soc.* **2007**, 129, 13713.
- (6) Straus, S. K. *Philos. Trans. R. Soc., B* **2004**, 359, 997.
- (7) McPherson, A. *J. Struct. Funct. Genomics* **2004**, 5, 3.
- (8) Bizzarri, A. R.; Bonanni, B.; Costantini, G.; Cannistraro, S. *ChemPhysChem* **2003**, 4, 1189.
- (9) Min, Q.; Pang, Y.; Collins, D. J.; Kuklev, N. A.; Gottselig, K.; Steuerman, D. W.; Gordon, R. *Opt. Express* **2011**, 19, 1648.
- (10) Zhu, C.; Meng, G.; Huang, Q.; Zhang, Z.; Xu, Q.; Liu, G.; Huang, Z.; Chu, Z. *Chem. Commun. (Camb.)* **2011**, 47, 2709.
- (11) Li, J.; Xu, X.; Wang, B.; Wang, Y.; Wang, L.; Zhang, C.; Sun, J. *J. Nanosci. Nanotechnol.* **2010**, 10, 7774.
- (12) Maier, S. A. *Plasmonics: Fundamental and Applications*; Springer Science + Business Media LLC: New York, 2007.
- (13) Gopinath, A.; Boriskina, S. V.; Reinhard, B. M.; Dal, N. L. *Opt. Exp.* **2009**, 17, 3741.
- (14) Shanmukh, S.; Jones, L.; Driskell, J.; Zhao, Y.; Dluhy, R.; Tripp, R. A. *Nano Lett.* **2006**, 6, 2630.
- (15) Boca, S.; Rugina, D.; Pinte, A.; Barbu-Tudoran, L.; Astilean, S. *Nanotechnology* **2011**, 22, 055702.
- (16) Stranahan, S. M.; Willets, K. A. *Nano Lett.* **2010**, 10, 3777.
- (17) Dieringer, J. A.; Lettan, R. B.; Scheidt, K. A.; Van Duyne, R. P. *J. Am. Chem. Soc.* **2007**, 129, 16249.
- (18) Jiang, J.; Bosnick, K.; Maillard, M.; Brus, L. *J. Phys. Chem. B* **2003**, 107, 9964.
- (19) Keating, C. D.; Kovaleski, K. K.; Natan, M. J. *J. Phys. Chem. B* **1998**, 102, 9414.
- (20) Hao, E.; Schatz, G. C. *J. Chem. Phys.* **2004**, 120, 357.

- (21) Clery, C.; Renault, F.; Masson, P. *FEBS Lett.* **1995**, 370, 212.
- (22) Holt, R. E.; Cotton, T. M. *J. Am. Chem. Soc.* **1987**, 109, 1841.
- (23) Teperik, T. V.; Popov, V. V.; Abajo, F. J. G. d.; Abdelsalam, M.; Barlett, P. N.; Kelf, T. A.; Sugawara, Y.; Baumberg, J. J. *Opt. Express* **2006**, 14, 1965.
- (24) Maier, S. A. *Opt. Express* **2006**, 14, 1957.
- (25) Cole, R. M.; Baumberg, J. J.; Abajo, F. J. G. d.; Mahajan, S.; Abdelsalam, M.; Barlett, P. N. *Nano Lett.* **2007**, 7, 2094.
- (26) Kho, K. W.; Shen, Z. X.; Olivo, M. C. *Opt. Express* **2011**, 19, 10518.
- (27) Strahler, A. N. In *Science and Earth History*; Prometheus Books: New York, 1999.
- (28) Stryer, L. In *Biochemistry*; W. H. Freeman and company: New York, 2000; pp 529–558.
- (29) Hildebrandt, M. S. P. *Biochemistry* **1989**, 28, 6710.
- (30) Ow, Y.-L. P.; Green, D. R.; Hao, Z.; Mak, T. W. *Nat. Rev. Mol. Cell Biol.* **2008**, 9, 532.
- (31) Zhou, J.; Jiang, S. J. *Phys. Chem. B* **2004**, 108, 17418.
- (32) Edmiston, P. L.; Lee, J. E.; Cheng, S. S.; Saavedra, S. S. *J. Am. Chem. Soc.* **1997**, 119, 560.
- (33) Lee, J. E.; Saavedra, S. S. *Langmuir* **1996**, 12, 4025.
- (34) Dick, L. A.; Haes, A. J.; VanDuyne, R. P. *J. Phys. Chem. B* **2000**, 104, 11752.
- (35) Herr, B. R.; Mirkin, C. A. *J. Am. Chem. Soc.* **1994**, 116, 1157.
- (36) Prime, K. L.; Whitesides, G. M. *Science* **1991**, 252, 1164.
- (37) Shafer-Peltier, K. E.; Haynes, C. L.; Glucksberg, M. R.; VanDuyne, R. P. *J. Am. Chem. Soc.* **2002**, 125, 588.
- (38) Dieringer, J. A.; McFarland, A. D.; Shah, N. C.; Stuart, D. A.; Whitney, A. V.; Yonzon, C. R.; Young, M. A.; Zhang, X.; VanDuyne, R. P. *Faraday Discuss.* **2006**, 132, 9.
- (39) Khoshtariya, D. E.; Dolidze, T. D.; Seifert, S.; Sarauli, D.; Lee, G.; Eldik, R. v. *Chem.—Eur. J.* **2006**, 12, 7041.